Available online at www.sciencedirect.com

jmr&t Journal of Materials Research and Technology

www.jmrt.com.br

Original Article

Characterisation of 17-4PH metallic powder recycling to optimise the performance of the selective laser melting process

*Pablo Zapico, Sara Giganto, Joaquín Barreiro, Susana Martínez-Pellitero**

Area of Manufacturing Engineering, Universidad de León, 24071 León, Spain

ARTICLE INFO

Article history:
Received 6 September 2019
Accepted 20 November 2019
Available online 9 December 2019

Keywords:
17-4PH stainless steel
Selective laser melting
Additive manufacturing
Powder bed fusion
Laser beam melting

ABSTRACT

The advantages of Additive Manufacturing (AM) processes are well known. Particularly, those AM techniques which are used to manufacture metallic parts are of great interest to industry due to the good mechanical behaviour of metallic alloys. Despite this, the quality of the manufactured parts is still an important issue due to the wide range of parameters that can affect them. In some powder bed fusion techniques, such as Selective Laser Melting (SLM), not all the initially distributed metallic powder is used in the process. There is an unmolten portion that can be recycled to ensure both the economic and environmental viability of the process. Even though this powder is unmolten, it is thermally affected due to the high temperatures attained during the process. This fact affects the powder properties and, consequently, the properties of the manufactured parts. Therefore, an analysis of the recycling effects of SLM metallic powders is an important issue in order to establish good recycling procedures and to optimise the process performance.

1. Introduction

Additive Manufacturing (AM) technology is increasingly relevant in industry due to the ability to manufacture very complex and customisable parts, especially in the medical, aerospace and automotive sectors [1]. Among the available AM techniques, those focussed on manufacturing metallic parts stand out due to the good mechanical properties of the parts, making it possible to use them as fully functional final parts. In this context, the most popular AM techniques are Laser Beam Melting (LBM), Electron Beam Melting (EBM) and Laser Metal Deposition (LMD). Depending on the manufacturer, the LBM process is also known as Selective Laser Melting (SLM) [2]. This process is based on selective laser fusion of a metallic powder bed by means of a high power-density laser.

One of the main reasons why these techniques have not been implemented as expected is the lack of available current standards [1]. Furthermore, it has been shown that the

* *Corresponding author.*
E-mails: pzapg@unileon.es (P. Zapico), sgigf@unileon.es (S. Giganto), jbarg@unileon.es (J. Barreiro), smarp@unileon.es (S. Martínez-Pellitero).

https://doi.org/10.1016/j.jmrt.2019.11.054

mechanical properties and quality of printed parts depend on the SLM process operation in relation to several factors, amongst them, the formation of pores, spatter, and denudation zones during the process [3–5]. These can lead to adverse effects on the mechanical properties, or the surface roughness of the manufactured parts, so decreasing their fatigue limit. On the other hand, during the SLM process the part is exposed to rapid heating for melting the powder followed by a fast solidification of the molten material. This complex thermal cycle causes the formation of residual stresses that produce negative effects on dimensional accuracy and crack formation [6].

Consequently, in recent years, the improvement of the general quality of SLM parts has been an important goal for researchers. Some works have already been carried out to analyse the general quality of the parts related to specific process parameters, raw material characteristics and post-process procedures. Parameters such as laser power, defocussing, laser scanning speed, hatch spacing, layer thickness, scanning strategy, build orientation, and working atmosphere have been analysed [7–10]. However, if the quality of the raw materials is not sufficiently characterised, it is difficult to ensure that the results obtained in these works can be reproducible. Some works have analysed the effect of the quality of the powder on the quality of the final manufactured parts [11–13]. In these studies, the initial powder underwent morphological (size, shape and superficial quality), chemical, and microstructural characterisation. These characteristics influence both the density and surface roughness of the manufactured parts [14]. Apart from characterisation, powder recycling is another factor to be analysed [15]. In the SLM technique, not all the powder on the build-up plate is used in the manufacturing process. There is an important portion of this powder that is unmolten and which can be recycled and reused. For this, the unused powder has to be sieved. This powder is thermally affected during the process, as demonstrated by the residual powder in the sieve. Recently, several works have evaluated the changes in the powder related to the number of recycling cycles, observing changes in the morphology and chemical composition, changes in the powder behaviour during the manufacturing process, and changes in the properties of the final parts. Insignificant changes in 4340 steel powders and their tensile properties were reported [16] when reusing the powder. Inconel 718 seems to be chemically stable after being reused several times [17], but its flowability reduces with recycling [18]. In the case of the titanium alloy Ti-6Al-4 V, the chemical composition of the powder changes with recycling, increasing the level of oxygen which reduces the mechanical properties of the final parts [19,20]. For Co-Cr alloy, 17-4PH [21], 316 L [14] and 304 L [22] stainless steels, both the particle size and the oxygen concentration increase during recycling, producing morphological and chemical changes. Another study reported that in addition to the recycling process, the storage time also increases the oxygen concentration [23]. Morphological changes in the powder affect the porosity, surface roughness, and the mechanical properties (such as fatigue or tensile behaviour) of the manufactured parts. The effect of the morphological characteristics of the powder on the SLM process is still not well understood, but it is related to the combination of several feedstock parameters including packing density, flowability, surface area, and thermal absorptivity [11]. According to this, it is important that the diameter of powder particles should be less than the layer thickness. The higher the sphericity and apparent density, the higher the density of the final parts; the lower the interstitial contaminants concentration, the better the layer adhesion and the mechanical properties of the manufactured parts. All of these properties are affected by powder recycling.

In this work, 17-4PH powder used in SLM process is characterised in three different states: (i) original state (or virgin state), (ii) after using and recycling 10 times and (iii) 20 times, respectively. The recycling process consists in recovering the unmolten powder by applying vacuum and sieving it in order to reload the powder store in the SLM machine. The three states of the powder were characterised morphologically, chemically, and microstructurally.

Table 1 – Commercial chemical composition of 17-4PH powder [26].

Element	Fe	Cr	Ni	Cu	Si	Mn	Nb
% of weight	Balance	15–17.5	3–5	3–5	<1.0	<1.0	0.15–0.45

2. Equipment and methodology

2.1. *SLM manufacturing process and metal powder sieving*

The SLM manufacturing process was carried out by means of a Direct Metal Printing ProX 100 SLM machine [24] distributed by 3DSystems. The main SLM parameters were setup according to previous work [25], that is, 38 W of laser power, 140 mm/s of scanning speed, 70 μm of hatch distance, and a layer thickness of 30 μm. The inert gas used during the manufacturing process was nitrogen. The sieving process was carried out by means of a 3DSystems PX-BOX connected to the SLM machine. This equipment allows the leftover powder, unused during the SLM process, to be vacuumed and sieved by means of a 75 μm mesh size sieve, in order to reuse it.

2.2. *Initial classification of the analysed powder*

The material used in the SLM manufacturing process was 17-4PH stainless steel powder, supplied by 3DSystems [26]. This alloy is usually used for small and high resistance structural components in the aerospace industry, as well as in marine environments, power plants and powder metal injection moulding industries, due to its excellent mechanical properties such as high tensile strength, fracture toughness, and corrosion resistance [26–28]. The chemical composition of this alloy is shown in Table 1.

In this study, the 17-4PH metallic powder was characterised in three different states related to the number of recycling cycles received: $\mathbf{P}_0$ (virgin powder, as received from the supplier), $\mathbf{P}_{10}$ (10 times recycled powder) and $\mathbf{P}_{20}$ (20 times recycled powder). The $\mathbf{P}_{20}$ powder was obtained after the sieving process, and just before loading the machine with new powder. Additionally, residual powder, $\mathbf{P}_R$, accumulated in the sieve of the PX-BOX has been analysed.

2.3. Powder analysis

2.3.1. Morphological analysis

The morphological analysis of the 17-4PH powder in the aforementioned states was carried out by means of Secondary Electron Imaging (SEI) obtained using a JEOL 6100 Scanning Electron Microscope (SEM). For this, 20 images, randomly distributed over a sample for each state of the powder, were taken using a 750x magnification. For each image, 50 random particles (selected using an algorithm developed by means of MATLAB) were analysed manually through ImageJ software. Therefore, 1000 particles were analysed for each powder state. The analysis was carried out manually, considering the roundness and aspect ratio of each particle, because of the unreliable results obtained by the automatic particle analysis system of ImageJ [29] observed in this case.

Moreover, a macroscopic morphological analysis was carried out using several images taken using a Leica KL 1500 LED plus microscope at 80x magnification.

2.3.2. Chemical composition analysis

The JEOL 6100 SEM equipment was also used to analyse the chemical composition evolution of the powder related to the number of recycled cycles. For that, an Energy Disperse X-Ray Spectroscopy (EDS) technique was used by means of the AZtec analysis software [30]. The oxygen concentration for each state of the powder was obtained by means of an Inert Gas Fusion Technique (IGFT) using a LECO analyser.

2.3.3. Microstructural analysis

The microstructure of the powder was determined using X-Ray Diffraction analysis (XRD), which allows the searching and matching of phases present in polycrystalline samples, such as those analysed in this work. A Bruker D8 Discover diffractometer, equipped with a Cu anode ($\lambda = 1.5418$ Å), was used to analyse both the virgin powder, $\mathbf{P_0}$, and the several times reused powder, $\mathbf{P_{20}}$. These tests were performed using a two-theta range of 40-100° at room temperature.

The powder used consisted of a ferrous alloy with approximately 73 % of Fe and a very low carbon content (Table 1), produced by means of gas atomisation [28]. This means that the phases which could be present are austenite, ferrite and martensite, with FCC, BCC, and BCT structures, respectively. Due to the low C concentration, the martensite structure, BCT, does not differ significantly from the ferrite structure, BCC [31]. Therefore, the XRD analysis enables the matching of the austenite (γ-phase, FCC) and ferrite/martensite (α/α'-phase, BCC), with these last two being mixed. Apart from this phase matching, the data obtained in the XRD analysis enables the relative proportions to be determined using the procedure described in the ASTM standard [32] for determining the retained austenite proportion, V_γ, in steel with a near random crystallographic orientation. This proportion can be calculated by means of Eq. (1).

$$V_\gamma = \left(\frac{1}{q}\sum_{j=1}^{q}\frac{I_{\gamma j}}{R_{\gamma j}}\right) \Big/ \left[\left(\frac{1}{p}\sum_{i=1}^{p}\frac{I_{\alpha i}}{R_{\alpha i}}\right) + \left(\frac{1}{q}\sum_{j=1}^{q}\frac{I_{\gamma j}}{R_{\gamma j}}\right)\right] \quad (1)$$

where:

Table 2 – Mean average diameter, maximum average diameter, mean roundness, and mean aspect ratio of the powder particles analysed for each powder state: P_0, P_{10}, P_{20} and P_R.

Powder State	$\overline{D_{AV}}$ (μm)	D_{AV}^{max} (μm)	$\bar{R}$ (%)	$\overline{AR}$ (%)
P_0	6.50	40.16	90.04	88.11
P_{10}	7.69	42.42	89.04	86.68
P_{20}	9.77	75.11	87.55	85.30
P_R	65.87	267.49	86.76	82.10

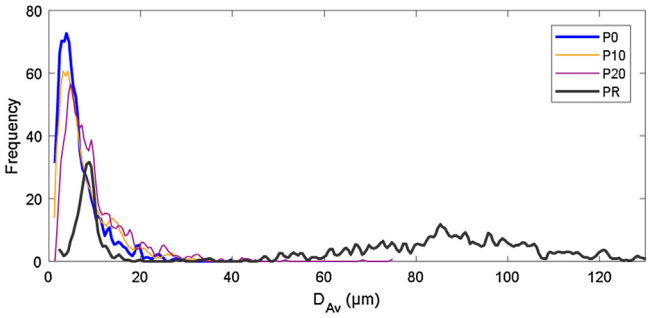

Fig. 1 – PSD related to the average diameters detected for each powder state: P_0, P_{10}, P_{20} and P_R.

I_α, I_γ : integrated intensities per diffraction peak in α/α' -phase and γ-phase,

p, q : number of diffraction peaks of α/α' -phase and γ-phase used.

The proportional parameter, R, permits the weighting of the integrated intensity for each peak. This parameter depends upon the interplanar spacing (hkl), the Bragg angle, crystal structure, composition of the phase being measured, X-Ray radiation, and temperature of the sample during the test. They can be calculated by means of tabulated values and other considerations of the test conditions [33].

3. Results and discussion

3.1. Morphological analysis

3.1.1. Quantitative analysis

The analysis of the SEI SEM images enabled the mean average particle diameters (D_{AV}), their maximum (D_{AV}^{max}), the mean roundness ($\bar{R}$), and the mean aspect ratio ($\overline{AR}$), to be obtained for all the particles analysed in each powder state, as shown in Table 2. $\bar{R}$ was calculated according to Eq. (2) and $\overline{AR}$ was calculated according to Eq. (3) with ImageJ, considering the powder particles as ellipses.

$$\bar{R} = 4 \cdot \frac{\text{Area}}{\pi \cdot (\text{Major Axis})^2} \quad (2)$$

$$\overline{AR} = \frac{\text{Major Axis}}{\text{Minor Axis}} \quad (3)$$

The particle size distribution (PSD) presented in Fig. 1 was obtained.

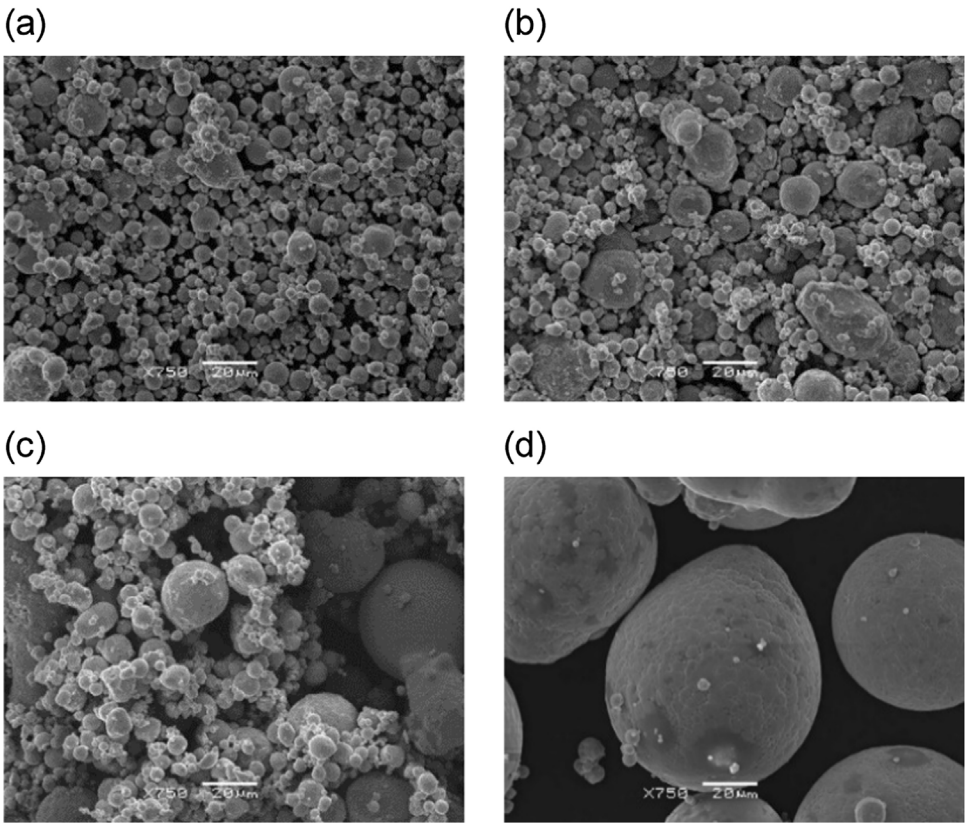

Fig. 2 – SEM images at 750x magnification: (a) P_0; (b) P_{10}; (c) P_{20}; (d) P_R.

The virgin powder, P_0, presented the smaller particle size, which increased when reusing the powder, as can be seen in the SEM images in Fig. 2. The residual powder, P_R, shows a larger size of particles than in the other powder states, such that this powder was discarded for additional use, staying in the PX-BOX sieve until it was removed in a periodical maintenance procedure. Therefore, this kind of powder, considered waste powder or non-appropriate powder, is not considered from this point on of the work.

In the case of the reused powder, the size of the particles evolved from an average diameter of 6.50 μm for the virgin powder, to 9.77 μm for the 20 times reused powder. Similar behaviour was observed in the case of the maximum average diameter, with an increase of 35 μm. The increase of the powder particle diameter is clear, but it can be seen that the average roundness and the average aspect ratio also changes. From the virgin powder, there is a decrease of 2.49 % in the roundness and a decrease of 2.81 % in the aspect ratio after 20 uses. These decrements are much less significant in the case of the 10 times reused powder, with a decrease of 1.00 % and 1.43 %, respectively.

The evolution in the size of the particles and their shape not only affects the morphologic characteristics of the powder, but also it can affect the correct operation of the SLM process and the quality of the manufactured parts. This can be explained by a reduction in the powder fluidity [34], which is affected by the agglomeration of small particles [21] and by the increase of irregularity in the particle's shape due to the rise of cohesive forces among them [35].

3.1.2. *Qualitative analysis: Evolution of particle's shape and texture*

The morphology of the virgin powder is due to the process by which the powder was produced. That is, spherical particles with smooth surfaces and small satellites attached to them are related to the gas atomisation process [21].

In Fig. 3, several kinds of particles can be observed, such as elongated, bonded, fractured, and rough textured.

Comparing Fig. 3, Fig. 4 and Fig.5, corresponding to the virgin powder, 10 times, and 20 times reused powder, respectively, the amount of irregular shaped particles, the agglomeration of particles, or molten particles with projections, increase with the powder reuse.

This morphological evolution may continue in the case that all the powder vacuumed from the SLM machine had been reused. The SEM analysis of residual powder images (Fig. 6) reveal that the main characteristics of highly reused powder are the same as those appearing, gradually, in the powder with each reuse. These are (Fig. 6): large sized particles (a); irregular shaped particles (b, c), some of them partially crushed because of the powder compaction roller action during the process; bonded particles (d); particle agglomerations (e, f); particles with molten projections (g, h) or satellites attached to them (i); as well as particles with cerebellar textures (a, h) amongst other irregularities.

Apart from the morphological evolution, the optical microscope images reveal colour changes in the powder (Fig. 7). The colour changes could be related to the increase of oxygen concentration due to oxide formation.

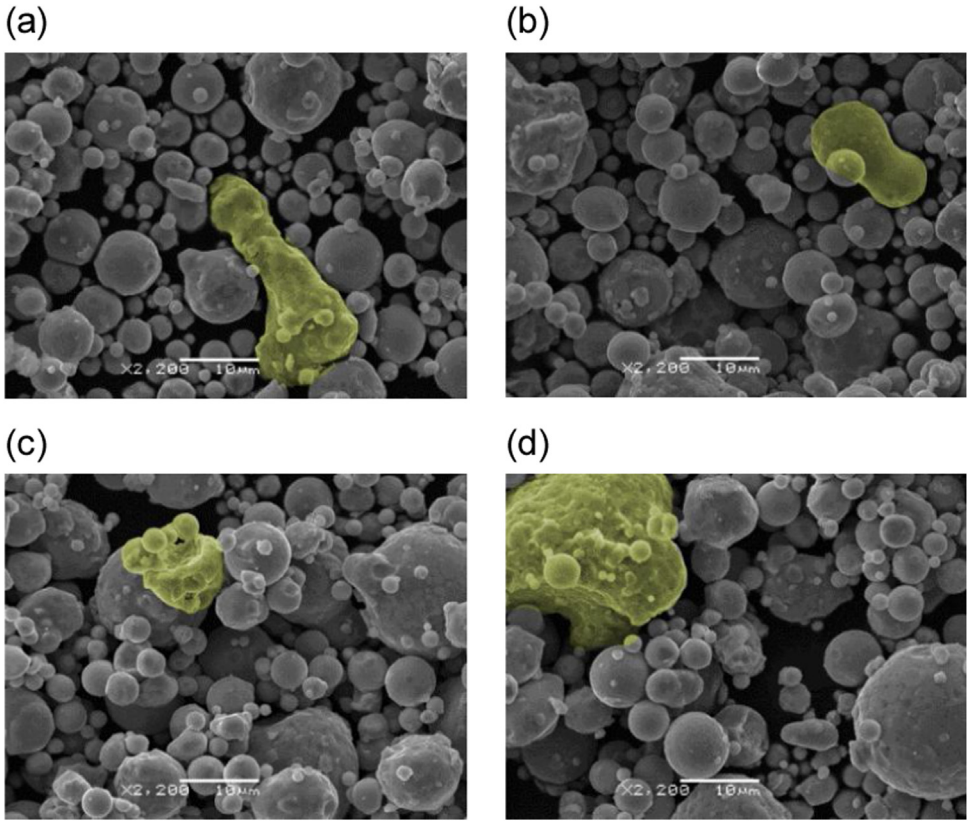

Fig. 3 – SEM images at 2200x magnification of the morphological features and peculiarities of the P_0 powder such as: (a) elongated particles; (b) bonded particles; (c) fractured particles; (d) particles with rough textures.

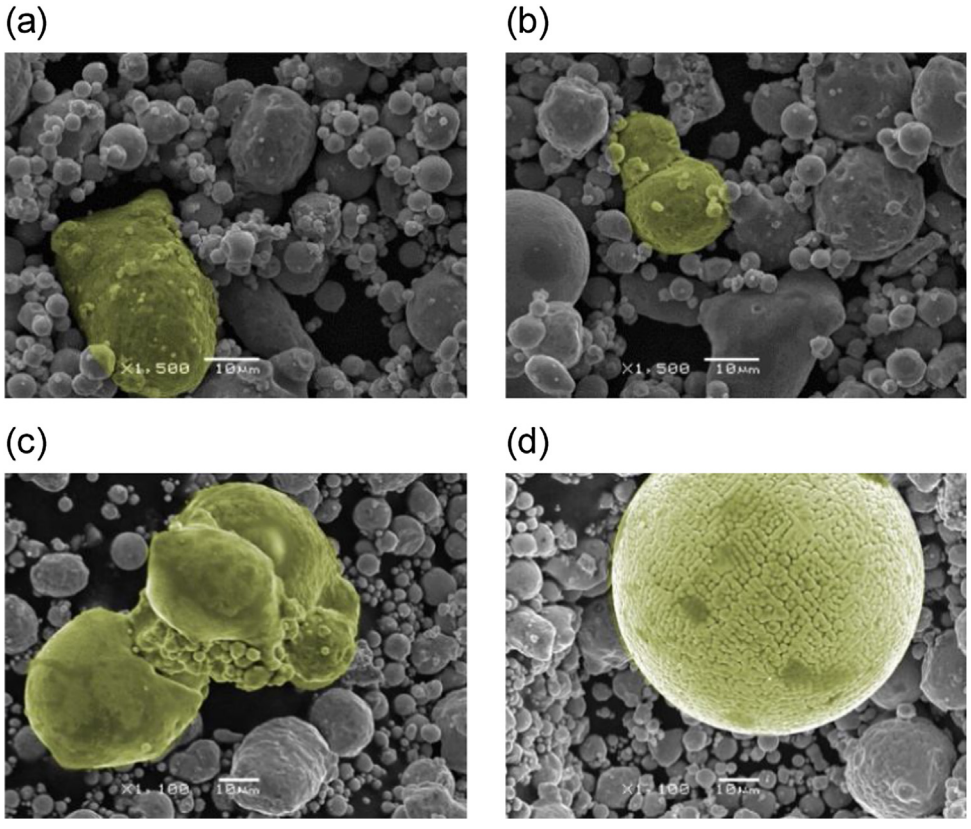

Fig. 4 – SEM images at 1500x and 1100x magnification of P_{10} powder features: (a) particles with irregular or elongated shapes; (b) bonded particles; (c) bonded particles accumulations; (d) particles with cerebellar textures.

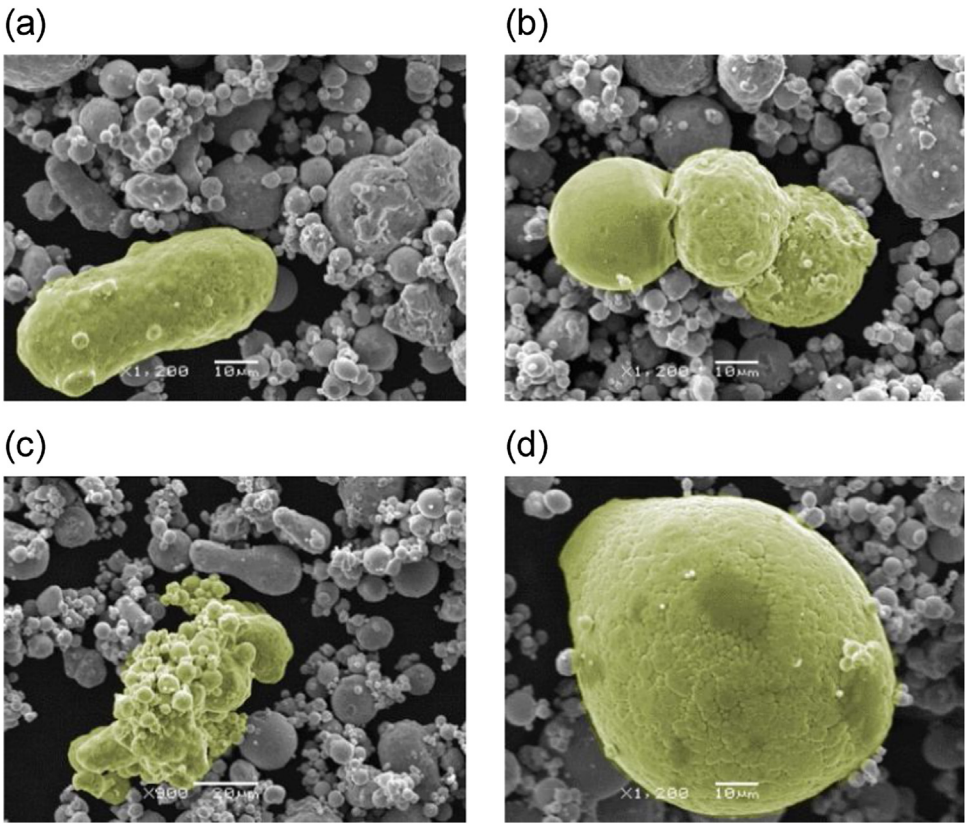

Fig. 5 – SEM images at 1200x and 900x magnification of P_{20} powder features: (a) particles with irregular or elongated shapes; (b) bonded particles; (c) bonded particles accumulations; (d) particles with cerebellar textures.

Table 3 – Oxygen, Carbon and Nitrogen content of the P_0, P_{10} and P_{20} powder states by means of LECO analyser.

Powder State	Composition in weight (%)					
	O	% variation	C	% variation	N	% variation
P_0	0.0970 ± 0.0006		0.0343 ± 0.00270		0.0731 ± 0.0006	
P_{10}	0.1104 ± 0.0062	13.8 %	0.0350 ± 0.00105	2%	0.0873 ± 0.0015	19.4 %
P_{20}	0.1070 ± 0.0074	10.3 %	0.0355 ± 0.00155	3.5 %	0.0873 ± 0.0017	19.4 %

3.2. *Chemical composition analysis*

The chemical composition analysis of the SLM powder (P_0, P_{10} and P_{20} state) was carried out in two ways. On the one hand, IGFT analysis was used in order to determine the concentration of oxygen present in the powder in each state, the results of which are shown in Table 3. This technique did not show the expected increase in oxygen due to the formation of oxides in the reused powder. The oxygen composition shown in the table is due to iron oxides formed during the contact of the powder with the oxygen present in air.

In addition to the oxygen concentration, this method also allows the determination of both the carbon and nitrogen concentrations in the powder. The XRD analysis states that the carbon concentration is very low and stable with reuse, both in phase matching and quantitative proportion. In addition, a concentration of nitrogen was also detected with this method and showed slight increases with powder reuse. This initial concentration in the virgin powder can indicate that the gas used during its atomisation was nitrogen. The increase of this element concentration with powder reuse can indicate that a proportion of nitrogen passes from the inert atmosphere, in the SLM machine chamber, to the powder during the manufacturing process. This result is interesting due to the well-known austenite stabilising character of nitrogen [36].

EDS analysis was carried out in order to determine the composition of the powder in the different states of reuse. In preliminary tests, it was observed that the composition of the powder particles mainly depends on their size. Therefore, for the EDS analysis the powder particles were classified in groups related to their sizes. In order to perform a full analysis of the powder, that is, in all the tested states, a complete PSD for P_0, P_{10} and P_{20} powder states was obtained (Fig. 8). This PSD allowed the classification of the particles in relation to their size, defining three groups marked by the terciles of the PSD, as shown in Table 4.

Once the powder particles were classified in size groups, an EDS analysis was carried out for 12 particles in each size group and in each powder state. The results are shown in Table 5. Different alloying elements of the 17-4PH steel were observed in

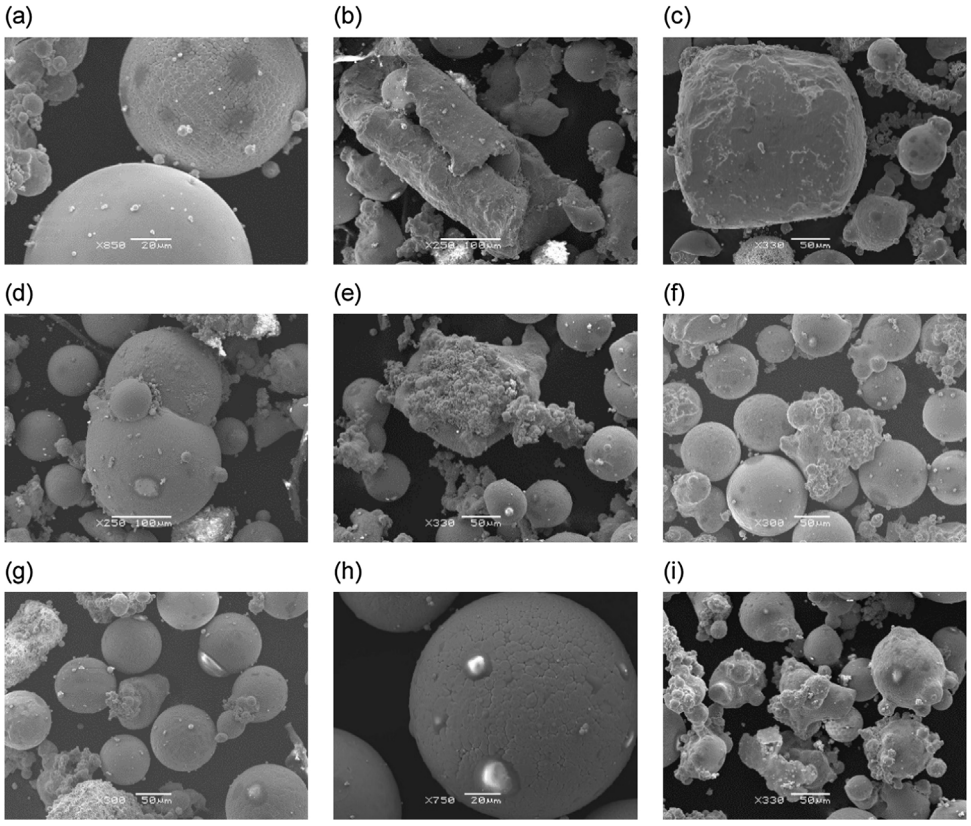

Fig. 6 – SEM images at 250x, 300x, 330x, 750x and 850x magnification of P_R powder features: (a) large particles with smooth or cerebellar textures; (b) particle with roll shape due to the roller action; (c) particle with irregular shape deformed by the manufacturing roller; (d) bonded particles; (e) and (f) accumulations of particles of different sizes; (g) and (h) particles with molten projections attached to them; (i) particles with satellites attached to them.

Table 4 – PSD classification groups.

Group	Diameter (μm)
G1	$Ø < 4.58$
G2	$4.58 \leq Ø \leq 8.35$
G3	$8.35 < Ø$

the powder (Table 1), except for niobium. This can be related to the low concentration of Nb in the 17-4PH steel. In addition, a notable concentration of oxygen was detected in the case of the G3 size group of reused powders (P_{10} and P_{20}) and an increase of Si and Mn was also observed. These combined increments could be related to the formation of both silicon and manganese oxides. The oxygen attributed to these oxides was not observed in the IGFT analysis because of their high thermodynamic stability.

In order to analyse the increase of oxygen, silicon and manganese concentration in the G3 size group of the reused powders, several composition maps were determined by means of JEOL SEM in combination with the Aztec software.

Table 5 – Average chemical composition (% of weight) of each size group (G1, G2 and G3) in each powder states (P_0, P_{10} and P_{20}).

		Averaged Chemical Composition (% of weight)							
Powder State	Group	Fe	Cr	Ni	Cu	Si	Mn	Nb	O
P_0	G1	72.2	17.5	4.4	4.4	0.8	0.8	–	–
	G2	72.0	17.8	4.4	4.2	0.7	0.8	–	–
	G3	72.0	18.0	4.3	4.1	0.7	0.9	–	–
P_{10}	G1	72.5	18.5	3.6	3.6	0.8	1.0	–	–
	G2	72.7	17.6	4.2	4.1	0.7	0.7	–	–
	G3	69.4	17.5	4.0	4.0	1.4	1.1	–	2.6
P_{20}	G1	72.5	17.7	4.0	4.2	0.8	0.8	–	–
	G2	72.4	17.8	4.1	4.0	0.7	0.8	–	–
	G3	67.6	17.8	3.7	3.8	1.7	1.6	–	3.9

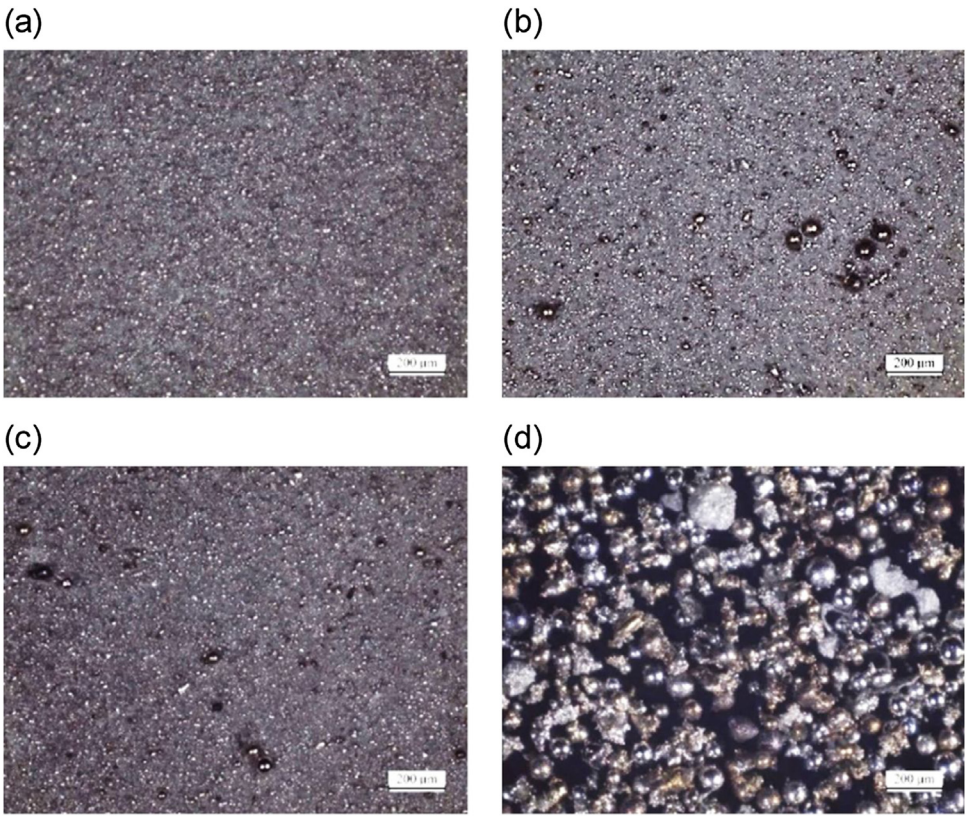

Fig. 7 – Microscope images at 80x magnification: (a) P_0; (b) P_{10}; (c) P_{20}; (d) P_R.

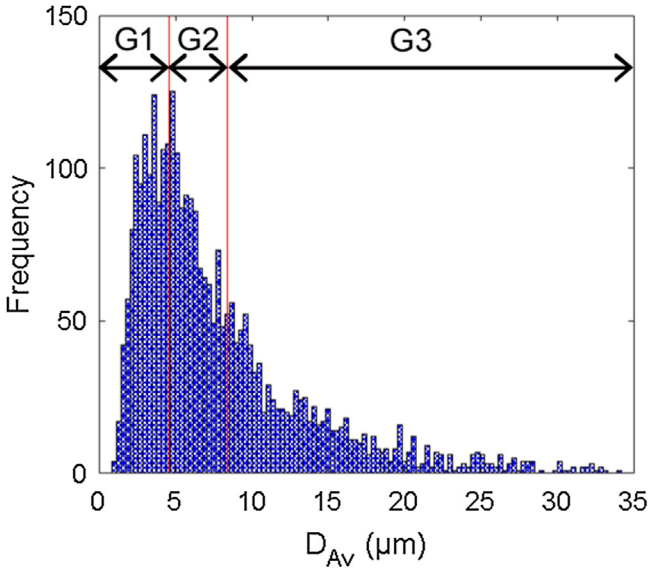

Fig. 8 – PSD (powder states P_0, P_{10} and P_{20}).

Due to the wide diameter values present in this G3 group (Fig. 8), the study was subdivided into three subgroups, also size related. For that, the diameters of analysed particles for this G3 group were isolated from the complete PSD, and new terciles were calculated for them. Table 6 describes the new subgroups.

The mapping procedure applied in these subgroups show that only the largest diameter particles contained oxygen (G3-C). Fig. 9 shows an example of one of the particles of the P_{10}-G3 state. It can be seen how the oxygen only appears in the subgroup G3-C. In this particle, it can be observed that the oxygen is distributed homogeneously.

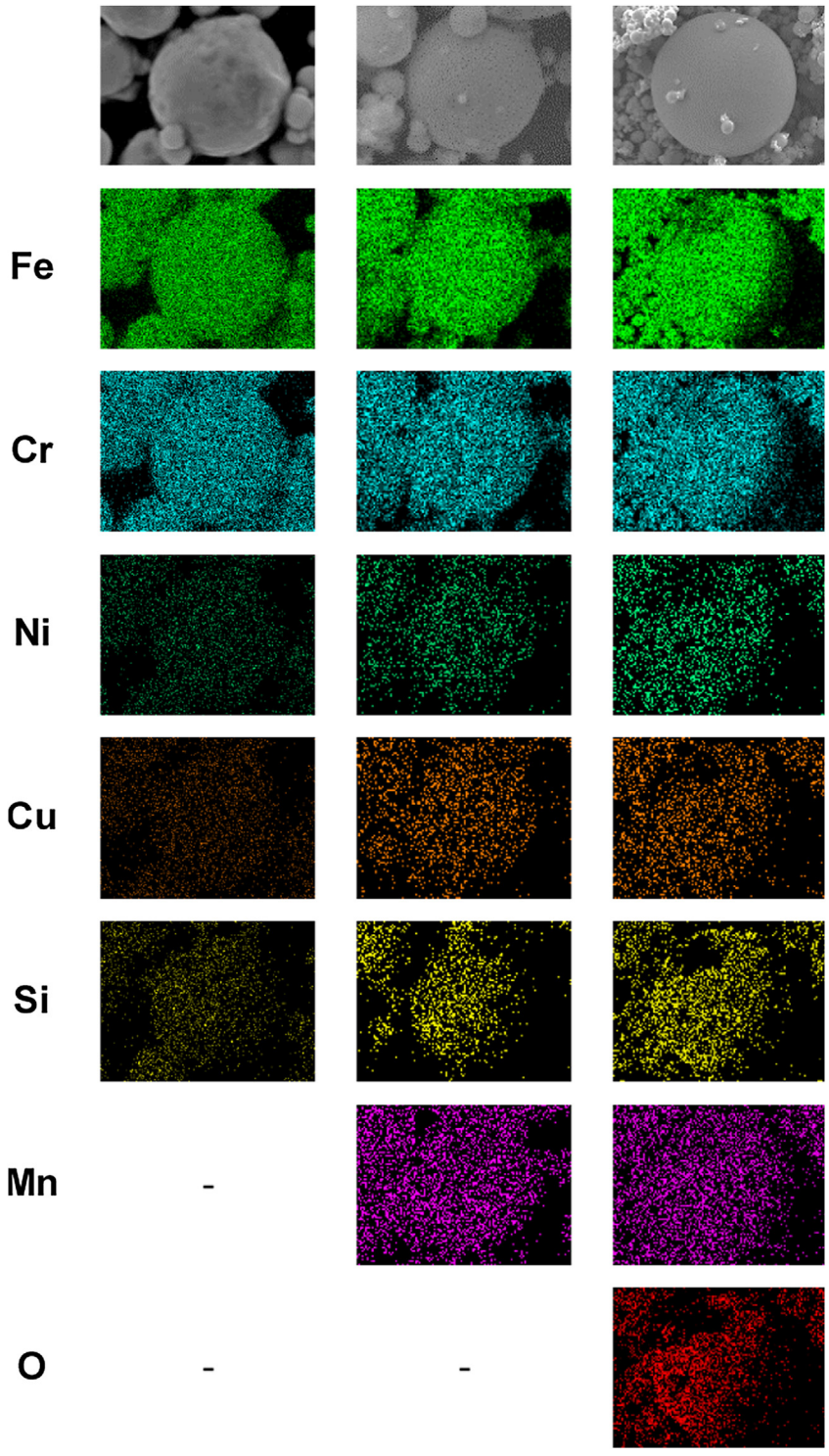

Fig. 9 – Mapping analysis of P_{10} powder particles corresponding to subgroup G3-A, G3-B and G3-C.

Table 6 – Classification subgroups of the G3 PSD.

G3 subgroups	Diameter (μm)
G3-A	$8.35 < Ø < 10.56$
G3-B	$10.56 \leq Ø \leq 15.14$
G3-C	$15.14 < Ø$

Through a more detailed analysis of particles in the G3-C group, it was observed that there were particles in which the oxygen was not homogeneously distributed. On the contrary, oxygen was localised in a well-defined area of the particle. This phenomenon can be observed in several different size particles as shown in Fig. 10, belonging to P_{10} and P_{20} powder states. Sometimes, these areas seem to be bubbles attached to

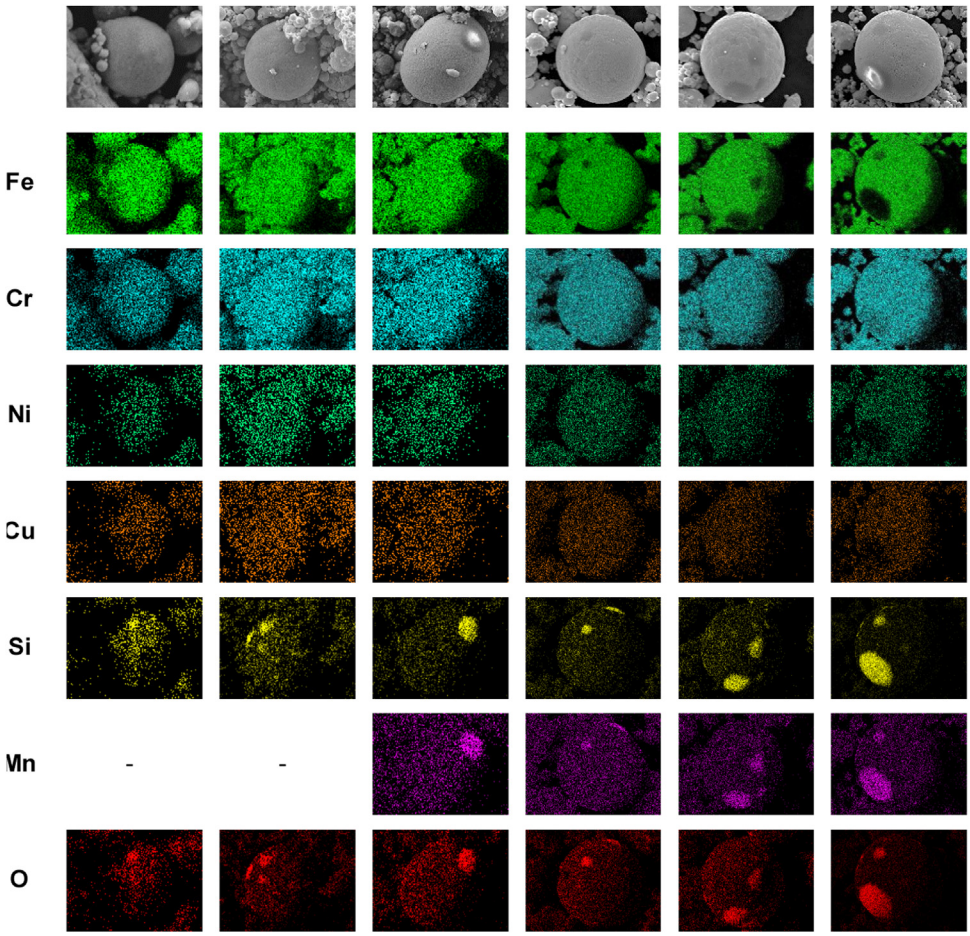

Fig. 10 – Mapping analysis of P_{10} and P_{20} powder particles with localised oxygen concentrations corresponding to subgroup G3-C: particles of small, medium and large size.

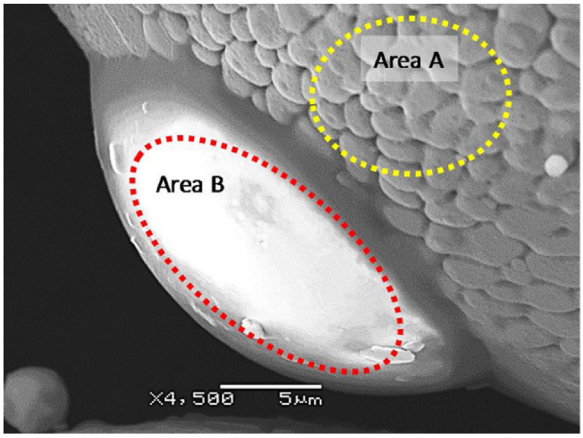

Fig. 11 – SEM images at 4500x magnification and EDS analysis of P_{10} powder particle with localized oxides concentration.

the particles (P_{10} medium size and P_{20} large size particles), so they could be formed as projections during the SLM process.

A more detailed analysis of this effect is shown in Fig. 11 for a P_{10}-G3C particle. As shown in the SEM image, there is a well-defined area of the particle (Area B) that has a very different composition than the rest of the particle (Area A). Observing the weight compositions of both areas, as happened with the G3 group particles of the reused powders, it can be seen that the oxygen, silicon and manganese concentrations are increased in Area B. Although most of the particle has a noticeable oxygen concentration, that is an oxide concentration, in this area the oxygen concentration increases dramatically. The composition of the area B can be explained by observing its atomic composition. The atomic concentration of oxygen can be explained, quite accurately, by the formation of oxides of all the alloying elements detected (less than 1 % error in the estimation of the oxygen concentration), that is, Fe_2O_3, Cr_2O_3, NiO, Cu_2O, SiO_2, and MnO_2. This does not apply in the case of the Area A. Thus, it can be stated that area B in this particle could be considered as a fully-oxidised area located within an also oxidised particle. Similar reasoning could be applied to P_{10} medium size and P_{20} large size particles shown in Fig. 10.

3.3. *Microstructural analysis*

The results of the XRD analysis of P_0 and P_{20} powder samples are represented schematically in Fig. 12a and Fig. 12b, respectively.

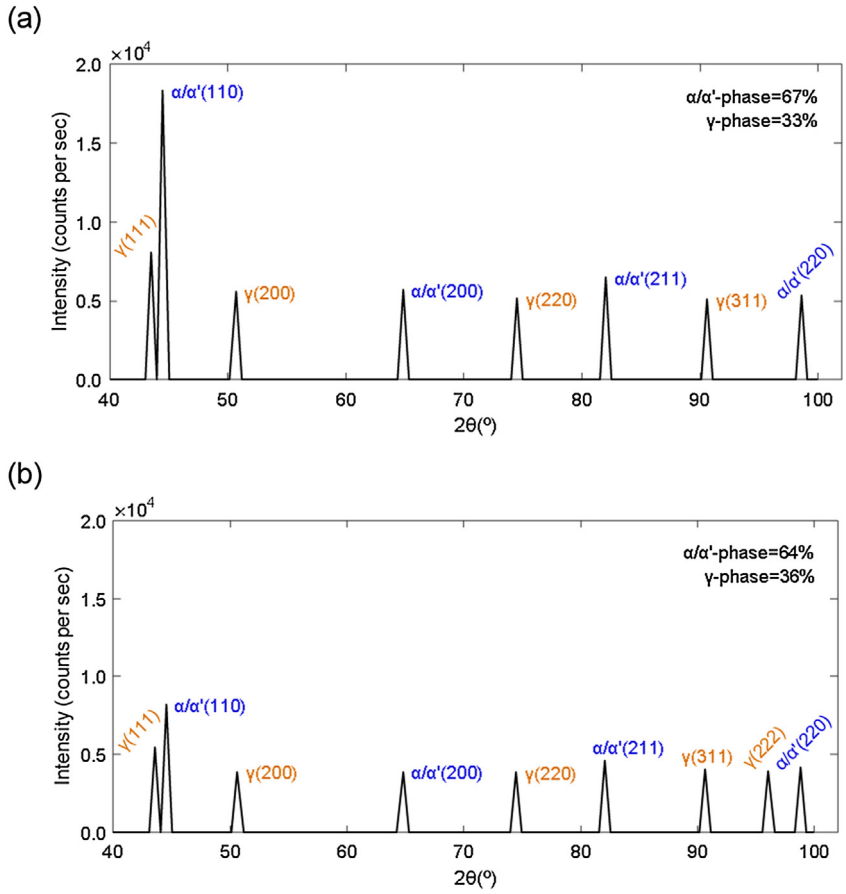

Fig. 12 – Schematic XRD results: (a) obtained for P_0 powder; (b) obtained for P_{20} powder.

As it can be observed, the phase proportions vary slightly when reusing the powder, with a slight increase of the γ-phase. This result agrees with other works that state a slight variation of the phase proportions occurs in the manufactured parts when using nitrogen as an inert gas in the chamber during the manufacturing process [28]. Nevertheless, in our work this is applicable to the powders which are thermally affected during the process. The austenite proportion remains almost constant due to the austenite stabilising characteristic of nitrogen. Even though this is a slight variation, it is notable due to the influence of the powder phase proportions on the mechanical properties of the final manufactured parts [12]. The number of powder reuse cycles is also an important issue to be considered.

4. Conclusions

In this work, 17-4PH stainless steel powder, used in a SLM additive manufacturing process, has been analysed in different grades of recycling. The aim is to characterise the changes suffered by the powder in order to determine the appropriate number of reuse cycles to ensure an optimal performance of the SLM process. For this, the stainless-steel powder was characterised morphologically, chemically, and microstructurally, in its original state, and after 10 and 20 manufacturing reuses. In order to reuse the unused powder during the SLM process, a recycling process was carried out, which consisted of vacuuming the powder, sieving, and reloading it in the machine powder store.

A morphological analysis of a large sample of particles was carried out by means of microscope image processing techniques, and which showed important changes in the powder after 20 reuses that could negatively affect the mechanical properties of the final manufactured parts.

Regarding the chemical composition of the powder, IGFT analysis showed stable concentrations of oxygen (due to thermodynamically stable oxides), carbon, and nitrogen, which were not described in the original powder specification. EDS analysis showed that chemical composition of the powder particles changed with reuse, with higher oxide concentrations appearing in the 15 μm larger particles (or distributed in a well-defined area).

Finally, XRD analysis showed a slight increment of the austenite phase with powder reuse which can be related to the austenite stabilising character of the inert gas used during the manufacturing process.

In summary, in this work morphological, chemical and microstructural changes of SLM 17-4PH powder have been demonstrated related to powder reuse. Due to the effect of these parameters on the production process, powder reuse is an important issue that has to be considered. It is recommended that the maximum number of powder reuse cycles be controlled, as well as to use finer mesh sieves due to the clear

relationship between the particle size and the oxides present in them.

Declaration of interests

The authors declare that they have no known competing financial interests or personal relationships that could have appeared to influence the work reported in this paper.

Acknowledgments

The authors gratefully acknowledge the financial support provided by the Junta de Castilla y León and FEDER (project ref. LE027P17). We also gratefully thank the Hedisa Group collaboration in the development of this research.

REFERENCES

[1] Campbell RI, Bourell D, Gibson I. Additive manufacturing: rapid prototyping comes of age. Rapid Prototyp J 2012;18(4):255–8.
[2] Herzog D, Seyda V, Wycisk E, Emmelmann C. Additive manufacturing of metals. Acta Mater 2016;117:371–92.
[3] Khairallah SA, Anderson AT, Rubenchik A, King WE. Laser powder-bed fusion additive manufacturing: physics of complex melt flow and formation mechanisms of pores, spatter, and denudation zones. Acta Mater 2016;108:36–45.
[4] Tang M, Pistorius PC, Beuth JL. Prediction of lack-of-fusion porosity for powder bed fusion. Addit Manuf 2017;14:39–48.
[5] Ponnusamy P, Masood SH, Ruan D, Palanisamy S, Mohamed OA. Statical analysis of porosity of 17-4PH alloy processed by selective laser melting. In: 2nd International Conference on Design, Materials and Manufacturing; 2017. p. 220.
[6] Cheng B, Shrestha S, Chou K. Stress and deformation evaluations of scanning strategy effect in selective laser melting. Addit Manuf 2016;(12):240–51.
[7] Wang Z, Xiao Z, Tse Y, Huang C, Zhang W. Optimization of processing parameters and establishment of a relationship between microstructure and mechanical properties of SLM titanium alloy. Opt Laser Technol 2019;112:159–67.
[8] Nguyen QB, Luu DN, Nai SML, Zhu Z, Chen Z, Wei J. The role of powder layer thickness on the quality of SLM printed parts. ACME 2018;(18):948–55.
[9] Rashid R, Masood SH, Ruan D, Palanisamy S, Rahman Rashid RA, Brandt M. Effect of scan strategy on density and metallurgical properties of 17-4PH parts printed by Selective Laser Melting (SLM). J Mater Process Technol 2017;249:502–11.
[10] Rakesh S, Raja A, Nadig P, Jayaganthan R. Influence of working environment and built orientation on the tensile properties of selective laser melted AlSi10Mg alloy. Mater Sci Eng 2019;750:141–51.
[11] Tan JH, Wong WLE, Dalgarno KW. An overview of powder granulometry on feedstock and part performance in the selective laser melting process. Addit Manuf 2017;18: 228–55.
[12] Averyanova M, Bertrand P, Verquin B. Effect of initial powder properties on final microstructure and mechanical properties of parts manufactured by selective laser melting. Annals of DAAAM for 2010 & Proceedings of the 21st International DAAAM Symposium; 2010.
[13] Sutton AT, Kriewall CS, Leu MC, Newkirk JW. Powders for additive manufacturing processes: characterization techniques and effects on part properties. Proceedings of the 26th Annual International Solid Freeform Fabrication Symposium–an Additive Manufacturing Conference; 2016.
[14] Heiden MJ, Deibler LA, Rodelas JM, Koepke JR, Tung DJ, Saiz DJ, et al. Evolution of 316L stainless steel feedstock due to laser powder bed fusion process. Addit Manuf 2019;25:84–103.
[15] Asgari H, Baxter C, Hosseinkhani K, Mohammadi M. On microstructure and mechanical properties of additively manufactured AlSi10Mg_200C using recycled powder. Mater Sci Eng A 2017;707:148–58.
[16] Jelis E, Clemente M, Kerwien S, Ravindra NM, Hespos MR. Metallurgical and mechanical evaluation of 4340 steel produced by direct metal laser sintering. J Min Met Mater Soc 2015;67(5):582–9.
[17] Ardila LC, Garciandia F, González-Díaz JB, Álvarez P, Echeverria A, Petite MM, et al. Effect of IN718 recycled powder reuse on properties of parts manufactured by means of selective laser melting. Phys Procedia 2014;56: 99–107.
[18] Nandwana P, Peter WH, Dehoff RR, Lowe LE, Kirka MM, Medina F, et al. Recyclability study on inconel 718 and Ti-6Al-4V powders for use in Electron beam melting. Metall Mater Trans B 2016;47(1):754–62.
[19] Strondl A, Lyckfeldt O, Brodin H, Ackelid U. Characterization and control of powder properties for additive manufacturing. JOM 2015;67:549–54.
[20] Tang HP, Qian M, Liu N, Zhang XZ, Yang GY, Wang J. Effect of powder reuse times on additive manufacturing of Ti-6Al-4V by selective Electron beam melting. JOM 2015;67:555–63.
[21] Slotwinski JA, Garboczi EJ, Stutzman PE, Ferraris CF, Watson SS, Peltz MA. Characterization of metal powders used for additive manufacturing. J Res Inst Stand Technol 2014;119:460–93.
[22] Sutton AT, Kriewall CS, Leu MC, Newkirk JW. Recyclability of 304L stainless steel in the selective laser melting process. Solid freeform fabrication 2018: proceedings of the 29th annual international. Solid freeform fabrication symposium – an additive manufacturing conference; 2018. p. 1311–26.
[23] Leung CLA, Marussi S, Towrie M, Atwood RC, Withers PJ, Lee PD. The effect of powder oxidation on defect formation in laser additive manufacturing. Acta Mater 2019;166:294–305.
[24] DSystems. Direct metal printers. Metal additive manufacturing with the ProX DMP 3D printers brochure; 2017.
[25] Zapico P, Giganto S, Martínez-Pellitero S, Fernández-Abia AI, Castro-Sastre MA. Influence of laser energy in the surface quality of parts manufactured by selective laser melting. Annals of DAAAM for 2018 & proceedings of the 29st international DAAAM symposium; 2018.
[26] DSystems. LaserForm 17-4PH (B) for ProX DMP 100, 200 and 300 Direct Metal Printers.
[27] Pasebani S, Ghayoor M, Badwe S, Irrinki H, Atre SV. Effects of atomizing media and post processing on mechanical properties of 17-4PH stainless steel manufactured via selective laser melting. Addit Manuf 2018;22:127–37.
[28] Murr LE, Martínez E, Hernández J, Collins S, Amato KN, Gaytan SM, et al. Microstructures and properties of 17-4PH stainless steel fabricated by selective laser melting. J Mater Res Technol 2012;1(3):167–77.
[29] Ferreira T, Rasband W. ImageJ user guide. Revised edition IJ 1.46r; 2012.
[30] Oxford Instruments. Aztec 4.0 user manual. Issue 2.1; 2013.
[31] Cheng L, Bottger A, ThH Kejser, Mittemeijer EJ. Lattice parameters of iron-carbon and iron-nitrogen martensites and austenites. Scr Metall Mater 1990;24(2):509–14.
[32] ASTM E975-13, Standard Practice for X-Ray Determination of Retained Austenite in Steel with Near Random Crystallographic Orientation.

[33] Waseda Y, Matsubara E, Shinoda K. X-ray diffraction crystallography: introduction, examples and solved problems. Springer Science & Business Media.; 2011.
[34] Gu D, Xia M, Dai D. On the role of powder flow behavior in fluid thermodynamics and laser processability of Ni-based composites by selective laser melting. Int J Mach Tools Manuf 2019;137:67–78.
[35] Yablokova G, Speirs M, Van Humbeeck J, Kruth JP, Schrooten J, Cloots R, et al. Rheological behavior of β-Ti and NiTi powders produced by atomization for SLM production of open porous orthopedic implants. Powder Technol 2015;283:199–209.
[36] Gu H, Gong H, Pal D, Rafi K, Starr T, Stucker B. Influences of Energy Density on Porosity and Microstructure of Selective Laser Melted 17-4PH Stainless Steel. 24th, Annual international solid freeform fabrication symposium; an additive manufacturing conference, Proceedings 2013; 2013. p. 474–89.